Energy & Environmental Science

PAPER

View Article Online
View Journal | View Issue

Cite this: *Energy Environ. Sci.*, 2018, **11**, 1287

A structurally versatile nickel phosphite acting as a robust bifunctional electrocatalyst for overall water splitting†

Prashanth W. Menezes,*[a] Chakadola Panda,[a] Stefan Loos,[b] Florian Bunschei-Bruns,[a] Carsten Walter,[a] Michael Schwarze,[a] Xiaohui Deng,[a] Holger Dau*[b] and Matthias Driess*[a]

The design and development of economical and highly efficient electrocatalysts for the hydrogen evolution reaction (HER) and oxygen evolution reaction (OER) under alkaline conditions are vital in lowering the overall energy losses in alkaline water electrolysis. Here we present a nickel phosphite, $Ni_{11}(HPO_3)_8(OH)_6$, belonging to the unique class of phosphorus-based inorganic materials with striking structural features that have been explored for the first time in the reaction of electrocatalytic overall water splitting with a profound understanding of the system using *in situ* and *ex situ* techniques. When electrophoretically deposited, the nickel phosphite exhibited remarkable electrocatalytic activity, yielding considerably low overpotentials for both the OER and HER with extreme structural stability and enhanced durability in alkaline media. Apart from the attractive structural merits, the higher activity of nickel phosphite is mainly attributed to the formation of oxidized nickel species in the catalytic OER process, while subtle experimental evidence of the participation of phosphite anions for the acceleration of the HER with the support of Ni^{2+} cations as catalytically active sites is identified, which is highly compelling and has never been previously discovered. Finally, the bifunctionality of nickel phosphite was demonstrated by constructing an alkaline water electrolyzer with a low cell voltage and over 4 days of undiminishing stability. This work offers an appealing cost-effective system based on earth-abundant metals for water electrolysis and can be extended to other transition metal based homo- or hetero-bimetallic phosphites.

Received 22nd December 2017,
Accepted 8th March 2018

DOI: 10.1039/c7ee03619a

rsc.li/ees

Broader context

Efficient overall water splitting into hydrogen and oxygen using inexpensive electrocatalysts that are highly active is a promising approach for the storage of renewable energy on a large scale and can potentially minimize or replace the currently used fossil-based fuels. Although the state-of-the-art candidates so far in this regard are catalysts based on noble metals, their exorbitant cost and scarcity limit their broader application. Hence the key challenge for the scientific world is to rationally design and synthesize catalytic materials based on first-row transition metals that can perform the oxygen evolution reaction (OER) and hydrogen evolution reaction (HER) efficiently in an environmentally benign and economically viable route. Presently, a robust bifunctional catalyst that furnishes both oxygen and hydrogen in a common reaction medium is highly desirable. The presented work describes the facile fabrication of electrocatalysts based on nickel phosphite ($Ni_{11}(HPO_3)_8(OH)_6$) material and their use for the first time as a bifunctional OER and HER and consequently overall water splitting electrocatalyst in alkaline media. The unique electronic and structural features allow them to achieve a greater extent of operational stability and excellent activity in terms of overpotentials and high current densities, which is an absolute requirement in the field of water splitting.

Introduction

With the rapid consumption of fossil fuels, the research and development of clean and sustainable energy resources to satisfy the need of energy demand have attracted great interest.[1–3] Alternatively, electrochemical water splitting into hydrogen (H_2) and oxygen (O_2) is widely regarded as a promising approach to producing environmentally-friendly fuel for future energy supply.[4–8]

[a] *Department of Chemistry, Metalorganics and Inorganic Materials, Technische Universität Berlin, Straße des 17 Juni 135, Sekr. C2, 10623 Berlin, Germany. E-mail: matthias.driess@tu-berlin.de, prashanth.menezes@mailbox.tu-berlin.de*

[b] *Fachbereich Physik, Freie Universität Berlin, Arnimallee 14, 14195 Berlin, Germany. E-mail: holger.dau@fu-berlin.de*

† Electronic supplementary information (ESI) available: Structural details; electrochemical activity measurements; and extensive microscopic, spectroscopic and analytical details of the materials before and after electrocatalytic experiments. See DOI: 10.1039/c7ee03619a

At the anode, water splits into O_2 gas through the oxygen evolution reaction (OER) with accompanying protons and electrons, and at the cathode, H_2 gas evolves through the hydrogen evolution reaction (HER) by the recombination of the protons and electrons.[9–12] Although noble metal-based electrocatalysts can function effectively for both the OER and HER, their scarcity and high-cost limit their widespread technological use.[13–16] In recent years, inexpensive, earth-abundant and environmentally benign transition metal oxides, hydroxides, chalcogenides, carbides, pnictides and alloys that could independently catalyze the OER and HER have been established.[17–31] Use of the same catalyst material at both electrodes (HER and OER) could provide additional advantages with respect to its facile applicability, *e.g.*, for deposition of both catalysts in one step by simultaneous coating of anodes and cathodes in integrated systems for light-driven water splitting. Discovering novel bifunctional electrocatalysts with exceptional electrocatalytic activity and stability in the desired media is highly demanding and has remained especially challenging.

Phosphorus-based materials have gained enormous attention since the discovery of cobalt phosphates (CoPi) by Nocera and co-workers in 2008, for the OER at near-neutral pH.[32,33] Structural characterization further revealed that CoPi resembles a layered-double-hydroxide structure, in which variable-charge metal–hydroxide sheets are separated by a hydrous interlayer region containing phosphate ions.[32–34] However, the interest in catalyzing the OER by a nickel–phosphate system is limited to a crystalline nickel phosphate ($NiPO_4$)[35] and hydroxide with interlayer phosphate (amorphous NiPi).[36] On the other hand, even though nickel phosphides were known to activate the HER,[37–40] they garnered much attention to be especially promising materials when the group of Lewis, in 2013, explored a nickel phosphide as a superior HER catalyst in acidic media.[41] Soon after, Stern and co-workers were able to investigate the same material for effective OER catalysis under alkaline conditions and demonstrated its overall water splitting capability.[42] Since then, varied compositions of nickel phosphides have been synthesized and studied as Janus catalysts for bifunctional HER and OER catalysis both in acidic and in alkaline media.[43–49] Recently, we discovered intriguing phenomena under alkaline OER conditions while investigating two nickel phosphides (Ni_2P and $Ni_{12}P_5$) where it underwent surface-structural rearrangement to form nickel phosphites and activated the catalyst.[50] Motivated by this, we aimed to probe an entirely novel class of materials, 'metal phosphites', for electrochemical overall water splitting.

Herein, to the best of our knowledge, for the first time, we have reported on a robust, structurally versatile, bifunctional nickel phosphite catalyst for alkaline electrochemical OER and HER, which exhibits remarkable activity and excellent stability both on nickel foam (NF) and on fluorine doped tin oxide (FTO). Simultaneously, using extensive analytical, microscopic and *in situ* and *ex situ* spectroscopic techniques, the compelling and unexpected structural aspects of the phosphites, their structure–activity relation, and the responsible active species have been established for each half-reaction (OER and HER). The alkaline-electrolyzer has been then assembled, demonstrating a low cell voltage and striking durability.

Results and discussion

Structural characterization of nickel phosphite

Nickel phosphite, $Ni_{11}(HPO_3)_8(OH)_6$, was synthesized using a mild-hydrothermal approach (see the Experimental section) and all of the diffraction peaks in powder X-ray diffraction (PXRD) patterns could be unambiguously assigned to the hexagonal phase (space group *P*63*mc*) with unit cell parameters a = 12.633 Å and c = 4.904 Å, confirming the high-purity of the product (Fig. S1, ESI†). The crystal structure consists of NiO_6 octahedra, where four oxygen atoms belong to $(HPO_3)^{2-}$ pseudo-tetrahedra and the rest of the oxygen atoms belong to hydroxyl groups, and is shown in Fig. 1a. Interestingly, each of the NiO_6 octahedra shares two of its edges with the next octahedron in the formation of $(NiO_4)_n$ zigzag chains. Condensation of four equivalent chains creates $(Ni_4O_{12})_n$ double chains along the *c*-axis (Fig. S2a, ESI†). Linking of such $(Ni_4O_{12})_n$ double chains by corner-sharing results in three-dimensional octahedral arrays (Fig. S2b, ESI†), which makes nickel phosphite a versatile material for catalysis.[51–53] The Brunauer–Emmett–Teller (BET) surface area of $Ni_{11}(HPO_3)_8(OH)_6$ is $\sim$17 $m^2\ g^{-1}$. The scanning electron microscopy (SEM) images exhibited the formation of a rod-shaped morphology with 1–2 μm

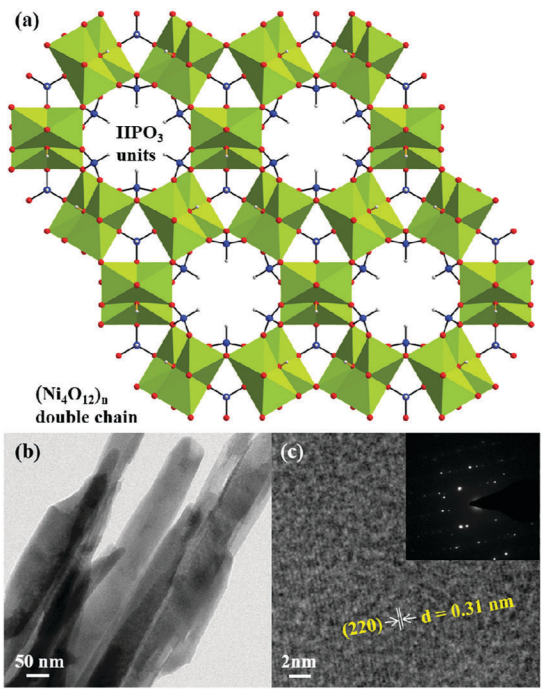

Fig. 1 (a) Crystal structure of $Ni_{11}(HPO_3)_8(OH)_6$ consists of zigzag $(Ni_4O_{12})_n$ double chains (represented by chartreuse octahedra) with $(HPO_3)^{2-}$ pseudo-tetrahedra (P: blue; O: red; H: grey) *via* corner-sharing (see Fig. S2, ESI,† and the main text for more details). (b) TEM image of $Ni_{11}(HPO_3)_8(OH)_6$ depicting a rod-type morphology. (c) The lattice fringes corresponding to the crystallographic plane (220) at d = 0.31 nm of the nickel phosphite phase were detected from the HR-TEM image and the respective SAED pattern is shown in the inset.

length and 50 nm diameter, which was further confirmed by transmission electron microscopy (TEM) studies (Fig. 1b and Fig. S3, S4, ESI†). The high-resolution (HR-TEM) analysis revealed the crystalline nature of rods and showed clear crystal planes with a lattice spacing of 0.31 nm, which corresponds to the (220) plane of the nickel phosphite (Fig. 1c).[51] Similarly, the reflection in the selected area electron diffraction (SAED) pattern could be perfectly matched with the planes of $Ni_{11}(HPO_3)_8(OH)_6$ (Fig. S4, ESI†). The composition and structure were additionally confirmed by inductively coupled plasma atomic emission spectroscopy (ICP-AES) and energy-dispersive X-ray analysis (EDX), while the O–H, P–O, P–H, H–P–O and Ni–OH vibrations were assigned by Fourier transform infrared (FT-IR) spectroscopy (Table S1 and Fig. S5, S6, ESI†).[54] The electronic structure of $Ni_{11}(HPO_3)_8(OH)_6$ was investigated by X-ray photoelectron spectroscopy (XPS). Both deconvoluted regions of Ni $2p_{3/2}$ and Ni $2p_{1/2}$ XPS exhibited a major peak at binding energies of 855.8 and 873.4 eV and could be assigned to the Ni^{2+} ($Ni(OH)_2$), whereas the minor peaks at 857.4 and 875.3 eV are attributed to the presence of Ni^{3+} in the structure (Fig. S7, ESI†).[35,55] The P 2p spectrum displayed a broad peak at 133.5 eV that confirms that all P atoms are in the +3 oxidation state (Fig. S8a, ESI†).[53,56] The O 1s spectrum could be deconvoluted into O1 and O2 peaks that are assigned to hydroxides and bound water of hydration (Fig. S8b, ESI†).[57] The results obtained here are consistent with reported nickel phosphites or nickel hydroxides.[53,55,56] The surface atomic Ni : P composition of the as-prepared material was 1 : 0.70 and is in accordance with ICP-AES (Table S1, ESI†). Detailed descriptions of the deconvoluted Ni 2p, P 2p and O 1s XPS analyses are given in the ESI† (Fig. S7 and S8).

Electrocatalytic OER and HER activities

The electrocatalytic OER performance of the nickel phosphite catalyst was evaluated using a typical three-electrode system in aqueous 1 M KOH electrolyte. Recently, nickel foam (NF) has become an attractive choice as an electrode substrate due to its 3D porous structure, low-cost, impeccable mechanical strength, greater corrosion resistance, and stronger and improved electrical conductivity. NF also has better adhesion properties, allowing faster ion and electron transport in comparison to other electrode substrates.[58–60] Therefore, the catalyst was first deposited electrophoretically on NF and used as working electrodes. Fig. 2a depicts the cyclic voltammogram (CV) of $Ni_{11}(HPO_3)_8(OH)_6$/NF; for comparison, those of noble metal-based RuO_2/NF, IrO_2/NF and Pt catalysts and bare NF were also measured under the same conditions. Of all, at an anodic geometric current density of 10 mA cm^{-2}, an overpotential of merely 232 mV was attained for $Ni_{11}(HPO_3)_8(OH)_6$/NF, whereas at 100 mA cm^{-2} the overpotential was only 362 mV (Fig. S9, ESI†). Strikingly, the OER overpotential acquired for nickel phosphite here is much lower than those of noble catalysts (see Table S3, ESI†) and one of the lowest in comparison to recently reported best-performing OER catalysts (Table S4, ESI†) and the nickel phosphite catalyst is top-notch among the earth-abundant OER catalysts.[5,10,17,25,61] The catalyst exhibited a distinct reversible redox peak between 1.2 and 1.4 V *versus* RHE, which is associated with the presence

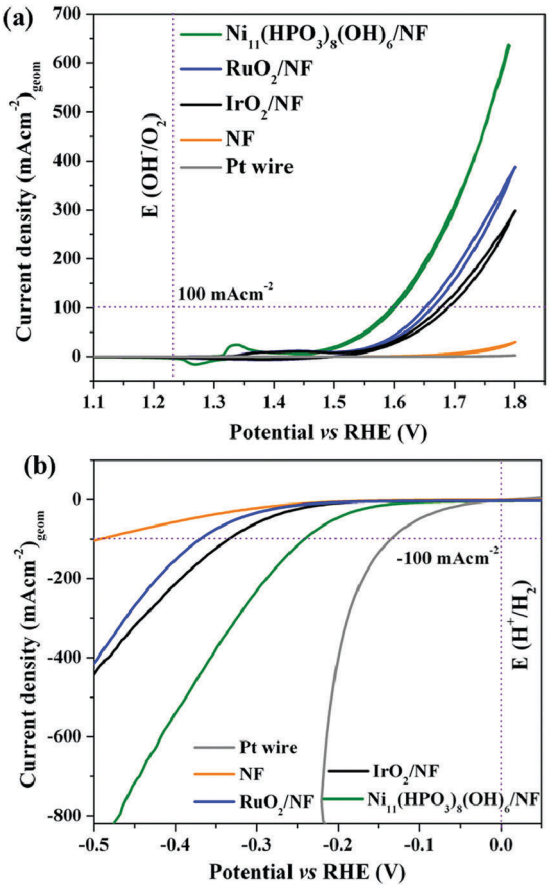

Fig. 2 The comparison of the (a) oxygen evolution (OER) and (b) hydrogen evolution reaction (HER) profiles of $Ni_{11}(HPO_3)_8(OH)_6$ and commercial noble metal-based catalysts. The catalytic performances were measured in aqueous 1 M KOH solution (sweep rate of 1 mV s^{-1} for the OER and 5 mV s^{-1} for the HER) using a three-electrode setup.

of Ni^{2+}/Ni^{3+} redox transition and is characteristic for Ni-containing OER catalysts, suggesting the formation of $Ni(OH)_2$/NiOOH (Fig. S10, ESI†).[62–64] The electrocatalytic kinetics of the OER were derived by extracting the slope from the Tafel plots. Fig. S11 (ESI†) presents the corresponding Tafel plots of the catalysts and the Tafel slope of the $Ni_{11}(HPO_3)_8(OH)_6$/NF catalyst for the OER was measured to be 91 mV dec^{-1}, which is lower compared to those of RuO_2/NF (118 mV dec^{-1}) and IrO_2/NF (128 mV dec^{-1}), indicating the favourable reaction kinetics in the OER process.

The chronoamperometric (CA) response of nickel phosphite was measured by maintaining a constant geometric current density of 10 mA cm^{-2}, and excellent long-term stability over 25 h was achieved (Fig. S12, ESI†). After CA, a CV was measured again and compared with the initial CV to probe conservation in activity; however, neither substantial change in the overpotentials nor that in total current occurred (Fig. S13, ESI†). Subsequently, the nickel phosphite and noble-metal based catalysts were also deposited on FTO substrates and their respective OER activities were determined (Fig. S14, ESI†). Under the applied OER conditions, an overpotential of 246 mV was attained at 10 mA cm^{-2} for $Ni_{11}(HPO_3)_8(OH)_6$/FTO, which is emphatically

low when compared to the noble-metal based catalysts (RuO_2/FTO, IrO_2/FTO and Pt wire) on FTO (see Table S3, ESI†) and other first-row transition metal-based materials (Table S4, ESI†).[5,10,17,25,61,65] In addition, the pronounced reversible redox (between 1.2 and 1.4 V) peak of $Ni_{11}(HPO_3)_8(OH)_6$ on FTO is consistent with that of NF (Fig. S15, ESI†).[62–64] Yet again, the catalyst was exceptionally stable over 24 h in OER CA (Fig. S16, ESI†).

We investigated the electrocatalytic HER performance of $Ni_{11}(HPO_3)_8(OH)_6$/NF in an alkaline environment. For comparison, the catalytic activities of Pt wire, RuO_2/NF, IrO_2/NF and bare NF were also tested and the linear sweep voltammograms (LSVs) are shown in Fig. 2b. As expected, the Pt wire exhibits the best HER activity with overpotentials of 42 and 130 mV at −10 and −100 mA cm^{-2}, respectively, whereas $Ni_{11}(HPO_3)_8(OH)_6$/NF was also competent with Pt and displayed overpotentials of 121 and 274 mV at the same current values (Fig. S17, ESI†). The HER activity of nickel phosphite was outstanding compared to those of commercial noble metal catalysts (Table S3, ESI†) measured on NF under similar conditions and clearly superior to those of most of the transition metal-based catalysts measured on NF (Table S5, ESI†).[5,9,17,18,28] The Tafel-slope of $Ni_{11}(HPO_3)_8(OH)_6$/NF was 102 mV dec^{-1}, which is significantly lower than those of RuO_2/NF (135 mV dec^{-1}) and IrO_2/NF (112 mV dec^{-1}) but higher than that of the Pt wire (90 mV dec^{-1}), and is shown in Fig. S18 (ESI†).

Apart from the electrocatalytic activity, proficient long-term stability was also achieved without losing much current density over 24 h in HER CA (Fig. S19, ESI†). Surprisingly, the initial LSV curve and the LSV measured after CA directly overlapped with each other, suggesting the extreme stability of $Ni_{11}(HPO_3)_8(OH)_6$/NF (Fig. S20, ESI†). The nickel phosphite and other noble metal-based catalysts were also deposited on FTO and measured under similar conditions (Fig. S21, ESI†); the $Ni_{11}(HPO_3)_8(OH)_6$/FTO exhibited an overpotential of 336 mV, which is rather far from that of the traditional Pt catalyst but favourable when compared to other commercial noble (RuO_2/FTO, IrO_2/FTO) and non-noble catalysts on FTO (Tables S3 and S4, ESI†). The measured CA responses indicated that the $Ni_{11}(HPO_3)_8(OH)_6$/NF catalyst exhibited significant stability in the first few hours and subsequently lost about 20% of its activity after 24 h (Fig. S22, ESI†).

Ex situ post catalytic characterization

Insights into the structure, morphological transformation, surface-structure reorganization, and structure–activity relation followed by in-depth information on the active sites resulted from studying each half-reaction electrode before and after electrocatalytic operation (OER CA and HER CA) individually by EDX, ICP-AES, TEM, HR-TEM, fast Fourier transform (FFT), XPS and quasi *in situ* X-ray absorption spectroscopy (XAS). First of all, the presence of Ni^{2+} hydroxide species in the $(Ni_4O_{12})_n$ double chains of the crystal structure of $Ni_{11}(HPO_3)_8(OH)_6$ and the existence of Ni^{3+} species in the structure that spontaneously form $Ni(OH)_2$/NiOOH are considered to be prerequisites for active-site formation in OER catalysis. This has been observed in several nickel-based OER materials (Fig. S2, ESI†).[62–64] The formation of such surface-active metal–OOH sites following proton-coupled electron transfer (PCET) steps have been proposed as key steps for catalysts based on transition metal hydroxides and oxides undergoing the OER.[25,27,66–71] However, in materials other than oxides (*e.g.* chalcogenides, pnictides, *etc.*), the surface is first transformed into an oxide/hydroxide layer under highly oxidizing conditions accompanied by significant loss of surface elements; then water oxidation may follow the same mechanism as outlined above for oxide materials.[42,72] We hypothesize that the presence of the hydroxide group in the structure itself facilitates standard OER mechanisms and minimizes the need for catalyst activation by uncontrolled restructuring or general amorphization, thereby supporting catalyst robustness and long-term stability. Notably, in transition metal-based oxides, phosphides and even chalcogenides, it has been often illustrated in the literature that under alkaline OER and HER conditions, the dissolution of metal cations or anions from the catalyst surface transpires and is thought to be one of the key factors in increasing the activity by promoting vacancies, defects or disorder at the surface.[72,73] In the present case, however, ICP-AES of the electrolyte (post catalysis) showed negligible loss of Ni (0.16% in the OER and 0.08% in the HER) and P (0.42% in the OER and 0.28% in the HER) from the surface structure, suggesting the superior stability of the catalyst under strongly alkaline OER and HER conditions in keeping with the EDX (Fig. S23, ESI†) and XPS (see below) analyses of the material. Also TEM and HR-TEM analysis shows a largely unchanged particle morphology; the formation of an amorphous shell was not detected (Fig. 3a, b and Fig. S24, ESI†),

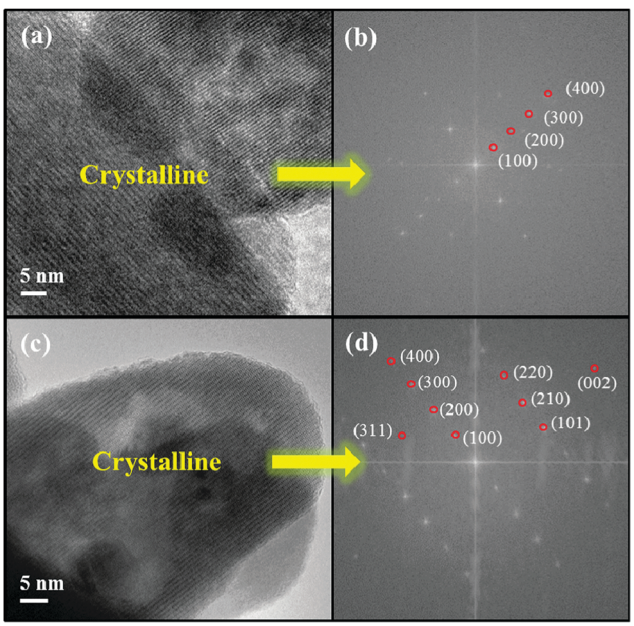

Fig. 3 HR-TEM (a and c) and the corresponding FFT (b and d) images of $Ni_{11}(HPO_3)_8(OH)_6$ after the OER CA and HER CA (24 h) in aqueous 1 M KOH, respectively. The particles were crystalline without the formation of any visible amorphous shell (clear crystalline borders), confirming the pronounced structural stability and sustainability of the catalysts in the strongly alkaline medium. In both cases, the HR-TEM images displayed clearly well-resolved lattice planes and the performed FFT generated spacing corresponding to the as-synthesized nickel phosphite. The hexagonal *P*63*mc* space group was used for indexing on the [010] zone axis.

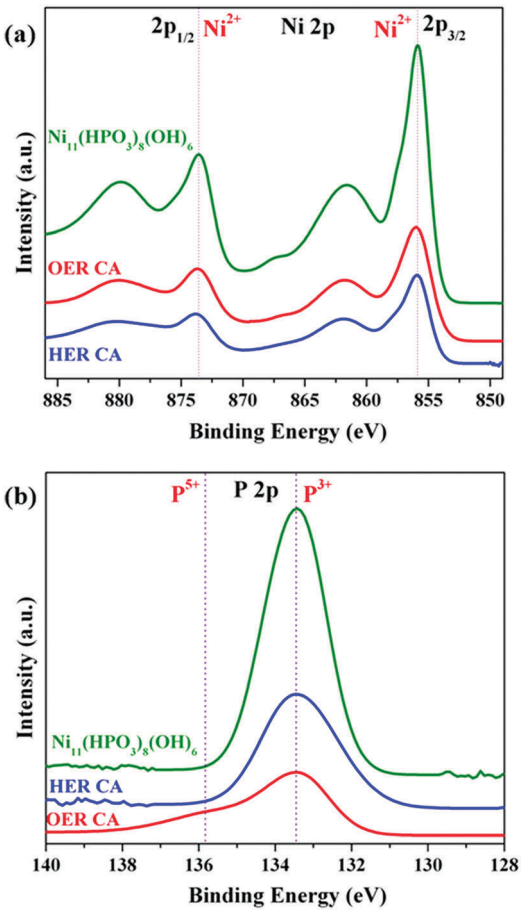

Fig. 4 The core-level (a) Ni 2p and (b) P 2p XPS spectra of $Ni_{11}(HPO_3)_8(OH)_6$, after OER CA and HER CA (24 h). No significant change in the Ni 2p or P 2p XPS spectra was observed apart from the minor oxidation of phosphors under OER CA conditions.

unlike those observed in other nickel-based materials where a thick amorphous shell frequently results from the OER in a strongly alkaline medium. Like in the OER also in the HER, the nickel phosphite was not transformed at the surface (Fig. 3c, d and Fig. S25, ESI†).

The Ni XPS spectra (Fig. 4) indicate the prevalence of Ni^{2+} and verify the absence of differences between the as-synthesized phosphite and the catalyst material after the OER and HER, evidencing the stability of nickel phosphite structures (see also Table S2 and Fig. S7 and S26, ESI†).[74] The phosphorus 2p spectra of both OER CA and HER CA showed a broad peak at ~133.2 eV corresponding to the +3 character of phosphorus that is consistent with the as-prepared phosphite structure (Fig. 4).[53,56] Interestingly, under OER CA, a small additional peak at 135.9 eV was also seen that reveals that the partial oxidation of P^{3+} to P^{5+} (Fig. S27, ESI†).[75] The O 1s was deconvoluted into 2 peaks (O1 and O2) corresponding to oxygen and hydroxide in phosphites and to bound water of hydration (for details see Fig. S28, ESI†).[53,57]

In situ X-ray absorption spectroscopy

To gather further structural insights into the chemical state, atom-specific chemistry and detailed local structural environment of

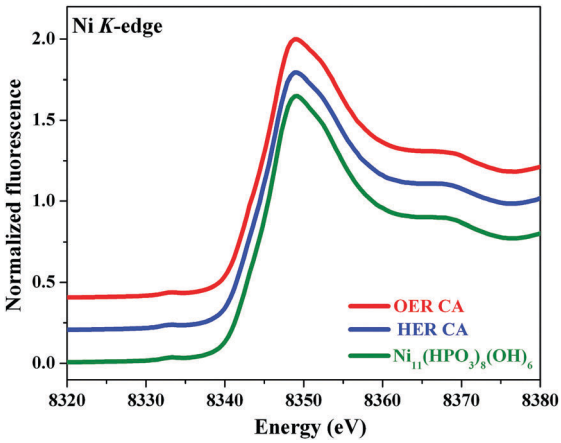

Fig. 5 XANES spectra of thin films of $Ni_{11}(HPO_3)_8(OH)_6$ recorded under quasi *in situ* conditions, as prepared, after OER CA and HER CA (24 h). In each case, the edge position revealed an average oxidation state of Ni of +2.1, confirming their dramatic structural stability under electrochemical conditions. The HER CA and the OER CA spectra have been shifted vertically by 0.2 and 0.4 for clarity.

nickel occurring in the particles during the OER and HER, quasi-*in situ* XAS was performed.[67,73,76,77]

Fig. 5 depicts the X-ray absorption near-edge structure (XANES) spectra of as-synthesized $Ni_{11}(HPO_3)_8(OH)_6$ along with the materials operated under OER- and HER-conditions. The mean oxidation state of Ni atoms (edge position) is almost identical for the three investigated catalysts. Accordingly, the oxidation state of Ni is found to be ~2.1 (see Table S6, ESI†), which is further supported by the simulation (bond valence sum) of the Ni EXAFS spectra (Table S7, ESI†).[66,78] From XANES spectra, it seems that the available Ni^{2+}/Ni^{3+} in nickel phosphite is sufficient to perform OER catalysis (Ni^{3+} might be enriched at the surface), whereas the presence of phosphite anions is largely responsible to carry out the HER efficiently.[79–81] In the Fourier-transform (FT) of the EXAFS spectra (k^3-weighted χ spectra are illustrated in Fig. S29, ESI†), only minimal transformation was observed for OER CA or HER CA (Fig. 6).

The first FT peak represents Ni–O distances from Ni–O octahedra;[80–82] further peaks represent larger Ni–Ni and Ni–P distances (Fig. 6 and 7). For more details on the EXAFS analysis and simulation results, see the ESI,† Table S7. The EXAFS data verify that the atomic structure of the nickel phosphite corresponds to the crystal structure, before and after electrocatalytic measurements (OER CA and HER CA). The material did not suffer any major alteration. This finding signifies the extreme stability of the structure and is consistent with the interpretations deduced from the XPS, HR-TEM and SAED measurements.

Insights into the active structure

The phosphite dianion, $(HPO_3)^{2-}$, is a conjugate base of the phosphorous acid, $[(HO)_2P(H)=O]$, with phosphorus in the oxidation state +3, which lies between the classical functional inorganic materials of phosphides ($P^{\delta-}$), hypophosphites $(H_2PO_2)^-$ and phosphates $(PO_4)^{3-}$ with varying phosphorus valencies of $\delta-$ to +5 (see Fig. 8). It has been previously shown that

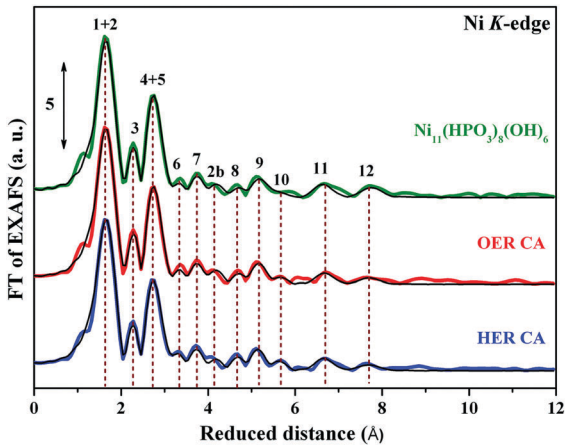

Fig. 6 Quasi *in situ* Ni K-edge FT of the EXAFS of $Ni_{11}(HPO_3)_8(OH)_6$, during OER CA and HER CA (24 h). Each peak in the Fourier transform relates to specific structural motifs that are schematically depicted in Fig. 7 and described in the main text. The spectra obtained by EXAFS simulations are shown as thin lines (simulation parameters are given in Table S7, ESI†). For convenience, the OER CA and HER CA spectra have been shifted vertically by an offset of −5 and −10, respectively.

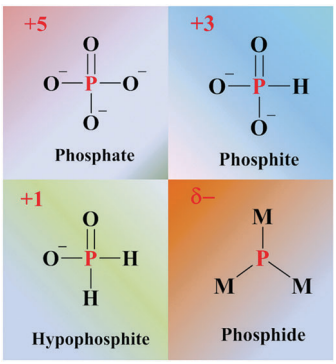

Fig. 8 Chemical structure elucidation of phosphorus based inorganic materials. The varying oxidation state of phosphorus is depicted in red.

polarization-induced partial negative charges localized on P atoms of a phosphide surface not only can trap positively charged protons to release H_2 during the electrochemical HER but also avert the system from deactivation.[17,18,24,83] The increasing amount of metal content in phosphides has proven to be beneficial for OER catalysis; however, P rich phases substantially improve the catalytic HER activity.[24,50,84] As the P atom is in an intermediate oxidation state of +3 in phosphite, it can accept protons and discharge them as H_2 gas in the presence of the applied reduction potential (electron supply) and revert to its resting state to continue the catalytic cycle. Therefore, we were intrigued to explore the influence of phosphites for HER catalysis as shown for phosphides.

On the other hand, metallic Ni has been widely studied for the HER for a long time, and recently, nano-sized alloys of Ni have been shown to be promising HER catalysts.[19] In nickel-based materials, it is usually expected that the $Ni^{\delta+}$ species undergo reduction under HER conditions, forming metallic Ni, which acts as a catalytically active site to adsorb protons and facilitate H_2 formation.[80,85,86] However, recently in $Ni(OH)_2$ and NiO based materials, it has been observed that apart from being a catalytic centre, the Ni^{2+} can also serve to enhance the first step of water dissociation (Volmer step, $H_2O + e^- \rightarrow H_{ad} + OH^-$).[19,81,87–90] Thus, the generated OH^- has an electrostatic affinity to the locally positively charged Ni^{2+} species (as it has sufficient unfilled d-orbitals) that can direct H^+ to adsorb on the second metal (non-metal in our case) atom.[19,81,87–90] As we did not detect any significant changes in the overall structure of phosphite and in the Ni^{2+} environment under reducing HER conditions in *ex situ*

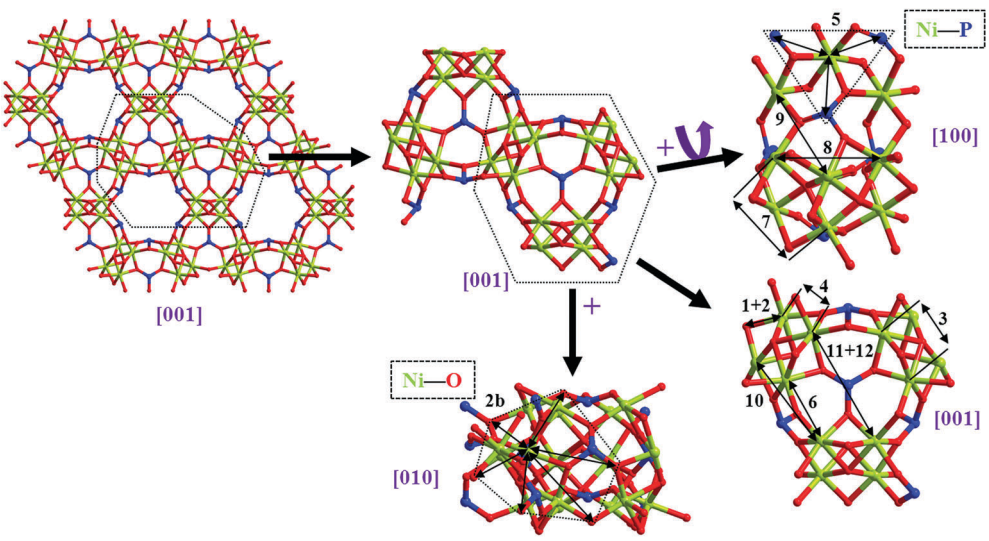

Fig. 7 Selected structural motifs of the $Ni_{11}(HPO_3)_8(OH)_6$ structure. The rod-like cavities along the [001] direction are shown on the left. The assignment of the motifs can be explicated by following the numbering of the Ni-scattered distances depicted on the right-hand side ([001], [010] and [100] directions) of the figure and in the FT of the EXAFS in the text (color code: chartreuse – nickel, blue – phosphorus, red – oxygen; hydrogen atoms are omitted for clarity).

and *in situ* conditions, we were keen to reveal the possible role of P centres in the HER.

We synthesized an innocent metal counterpart, zinc phosphite, $Zn_{11}(HPO_3)_8(OH)_6$, with an isotypic structure under mild hydrothermal conditions (Fig. S30, see Experimental, ESI†) such that we could directly infer the reduction ability of the phosphite anion. Such strategies are well documented in the inorganic molecular chemistry literature to encounter the redox behaviour of the surrounding ligand framework bound to a transition metal complex.[91,92] While investigating the HER of $Zn_{11}(HPO_3)_8(OH)_6$ in alkaline media, an overpotential of 175 mV at -10 mA cm^{-2} was obtained, whereas limited activity was exhibited for the OER compared to $Ni_{11}(HPO_3)_8(OH)_6$ (Fig. S32, ESI†). This implies that aside from acting as a catalytic site, Ni^{2+} promotes the faster dissociation process of water to provide protons that get discharged (H_{ad}) at the P centre in the presence of the applied reduction potential (Fig. 9). The evolution of H_2 from the P terminated surface can then be followed in two ways: (i) either two of the H_{ad} can combine to form H_2 and/or (ii) one of the H_{ad} combines with the existing structural H on the P centre to produce H_2 followed by regeneration of the original structure by an attack of additional protons from dissociated water molecules (Fig. S33, ESI†). We have mainly focused on the $Ni^{2+/3+}$ OOH based OER mechanism in the section on post-catalytic characterization; however, a cooperation involving the phosphite group acting as a proton buffer, as hypothesized in the HER mechanism, cannot be completely ruled out. The proposed mechanistic pathway also accounts well for our *in situ* and *ex situ* experimental observations towards the robustness of the material during and after the electrocatalytic reaction, supporting P centred catalysis that allows retention of the original structure (Fig. 9).

To further rule out all possible scenarios including the contribution of zinc and/or the electrode substrate to the net reactivity and to strengthen our hypothesis of P centred catalysis, we further compared $Zn_{11}(HPO_3)_8(OH)_6$ to that of a phosphate, $Zn_3(PO_4)_2(H_2O)_4$, synthesized by the precipitation method (Fig. S34, ESI†) and to commercial Zn powder (Fig. S35, ESI†).

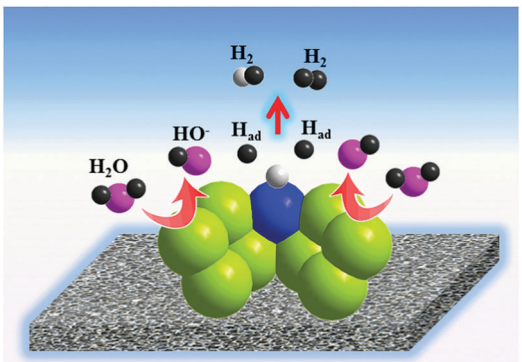

Fig. 9 Schematic illustration of the proposed HER mechanism of nickel phosphite based on the experimental elucidation. A space filled asymmetric model of the $Ni_{11}(HPO_3)_8(OH)_6$ where nickel octahedra are shown in chartreuse and the phosphite anion in blue with the structural hydrogen (grey) sitting on the P centre. Oxygen atoms are omitted for clarity.

The substantially higher catalytic activity of $Zn_{11}(HPO_3)_8(OH)_6$ was established over $Zn_3(PO_4)_2(H_2O)_4$, and Zn powder, highlighting the role of phosphites in improving catalytic activity in the HER and excluding the possible contribution of zinc (Fig. S36, ESI†). As expected, phosphites, phosphates and zinc powder were inactive for the OER (Fig. S37, ESI†). Moreover, at this point in time, we also propose that hypophosphites (see Fig. 8), having two H-atoms bonded to P centres, could also be considered as suitable and promising candidates to enhance the HER.

Based on the described *ex situ* and *in situ* measurements, we conclude that the exceptional electrochemical OER and HER activities and long-term stability of nickel phosphite result from (i) hydroxides coordinated to the $(Ni_4O_{12})_n$ double chains of nickel phosphite that facilitate the rapid –OOH intermediate formation needed for driving the OER,[64,78,93–95] (ii) the phosphite anion, which plays a key role in both maintaining the structure and at the same time providing structural flexibility, as previously documented for Co pyrophosphates,[96] (iii) the preservation of the morphology and crystallinity during the OER, without restructuring that results in a thick amorphous shell of $M(OH)_2$/MOOH,[62,63,66,73,97–100] (iv) the dual nature of Ni^{2+} during the HER, fostering water dissociation and assisting phosphite anions, $(HPO_3)^{2-}$, to act as base to accept protons with the subsequent release of H_2.

Alkaline water electrolysis

Based on the electrochemical investigation, it is apparent that the nickel phosphite represents an exceptional bifunctional OER and HER catalyst with impressive stability and predestined to be an overall water splitting catalyst. Therefore, we further assembled an alkaline electrolyzer both prepared with $Ni_{11}(HPO_3)_8(OH)_6$ on NF and used as an anode and a cathode in a two-electrode configuration. The LSV of the water electrolysis of $Ni_{11}(HPO_3)_8(OH)_6\|Ni_{11}(HPO_3)_8(OH)_6$ in aqueous 1 M KOH electrolyte solution at a sweep rate of 1 mV s^{-1} is shown in Fig. 10. The electrodes displayed excellent activity, reaching a water-splitting current density of 10 mA cm^{-2} upon applying only a cell voltage of 1.6 V, and the resulting catalytic activity could directly be correlated with the other current highly active bifunctional electrocatalysts reported in the literature.[101]

In addition to the catalytic activity, the long-term stability of the material is vital to achieving a high-grade cell for water splitting. Consequently, the chronoamperometric test was performed affording a potential of 1.65 V, which displayed stable current for a day and then a slight decrease in current each day owing to the evaporation of the electrolyte with slow deactivation but the addition of electrolyte to adjust the level of the electrode resulted in an increment in the current. Vigorous O_2 and H_2 bubble formation was also clearly seen on the cathode and anode during the entire electrolysis process (Fig. S38, ESI†). After the 4 days' stability test, the catalytic activity of the electrodes was further investigated, and impressively, no substantial decrease (1.62 V) in activity compared to the initial LSV was detected (Fig. S39, ESI†), demonstrating it to be one of the strongest contenders for future alkaline electrolysis. The Faradic

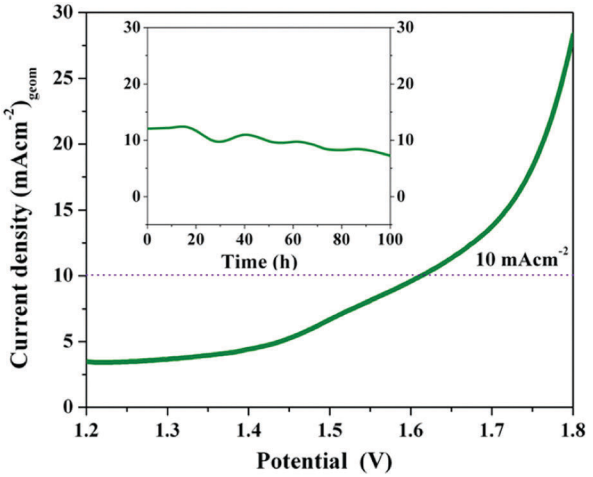

Fig. 10 LSV curve of the water electrolysis of nickel phosphite ($Ni_{11}(HPO_3)_8(OH)_6$||$Ni_{11}(HPO_3)_8(OH)_6$) on NF with a two-electrode configuration in aqueous 1 M KOH. The long-term stability measurement by applying a cell voltage of 1.65 V is shown in the inset (see the main text for details).

efficiency (FE) and the relative evolution rates of H_2 to O_2 were obtained by analyzing and quantifying the head-space gas samples of electrolysis (performed in a closed electrochemical cell) by gas chromatography (GC) and mass spectrometry (MS). The FE obtained as per GC measurements was ~100% for the HER and ~95% for the OER (see the ESI;† Table S8). Interestingly, the ratio of H_2 to O_2 evolved as observed by the MS analysis of the head-space gas samples was 2 : 1 that renders the efficient selectivity of the catalyst towards both half-cell reactions (Fig. S40, ESI†). Further, to support the MS study, *i.e.* the observed ratios, an inverted electrochemical cell (graduated) was used such that the evolved H_2 and O_2 could be collected separately at atmospheric pressure to directly infer the volumes and the ratios of the respective gases evolved (for more details see Fig. S41, ESI†). The volume ratio obtained for H_2 and O_2 in this way was also 2 : 1 (Fig. S42, ESI†). To strengthen our claim on the extremely high stability (based on 4 days of the CA experiment) of the catalyst, we determined the FE of the used catalyst towards the HER and OER that yielded similar results to those of the as-prepared catalysts. The TEM measurements after the electrolysis experiment (Fig. S43, ESI†) showed retention in the crystallinity of the catalysts, suggesting sustainability under in the long-run.

Conclusions

In summary, a unique type of material, nickel phosphite ($Ni_{11}(HPO_3)_8(OH)_6$), has been introduced as a bifunctional OER/HER catalyst for electrochemical overall water splitting. The structurally versatile nickel phosphite electrophoretically deposited on electrode substrates exhibits remarkable electrocatalytic activity, durability and unexpected structural stability for both the OER and HER under intense alkaline conditions. The formation of oxidized nickel species at the near surface of the catalyst is indispensable to catalyze the OER efficiently, whereas, for the first time, we have experimentally elucidated the participation of phosphite $(HPO_3)^{2-}$ anions with the assistance of Ni^{2+} cations for driving the HER. The corresponding two-electrode alkaline electrolyzer using nickel phosphite as both an anode and a cathode demonstrated to be an efficient system achieving a very low cell voltage and improved long-term stability. The presented work opens new avenues in utilizing rich metal phosphites as promising materials for electrochemical overall water splitting and gives also a hint on the structural suitability of hypophosphite materials for renewable energy production.

Experimental

Synthesis of nickel phosphite ($Ni_{11}(HPO_3)_8(OH)_6$)

Nickel phosphite was synthesized using a mild hydrothermal method. 1.320 g of nickel(II) chloride hexahydrate ($NiCl_2{\cdot}6H_2O$) and 0.640 g of ammonium dihydrogen phosphate ($NH_4H_2PO_4$) were taken in a 50 mL Teflon-lined stainless-steel autoclave and 30 mL of water was added to the mixture. The autoclave was then placed on a magnetic stirrer for 30 minutes to obtain a clear green solution. The autoclave was tightly sealed and heated at 220 °C for 24 h. After the completion of the reaction, the autoclave was cooled to room temperature naturally and the resulting green crystalline precipitate was separated by centrifugation (9000 rpm/10 min), and washed with distilled water (3 × 50 mL) and finally with acetone (3 × 50 mL), which was then dried overnight in air.

Synthesis of zinc phosphite ($Zn_{11}(HPO_3)_8(OH)_6$)

Zinc phosphite was also synthesized similar to nickel phosphite. 0.458 g of zinc(II) acetate dihydrate ($Zn(OAc)_2{\cdot}2H_2O$) and 0.794 g of sodium hypophosphite (NaH_2PO_2) were taken in a 50 mL Teflon-lined stainless-steel autoclave and 20 mL of water was added to the mixture. The autoclave was then placed on a magnetic stirrer for 30 minutes to obtain a colourless solution. The autoclave was tightly sealed and heated at 160 °C for 24 h. After the completion of the reaction, the same above procedures were followed to obtain a colourless crystalline product. The structural and compositional characterization studies were conducted by PXRD and ICP-AES analysis to check the phase purity of the product.

Synthesis of zinc phosphate ($Zn_3(PO_4)_2(H_2O)_4$)

Zinc phosphate was synthesized by a solution-based precipitation method. $Na_3PO_4{\cdot}12H_2O$ (0.61 g) and $Zn(OAc)_2{\cdot}2H_2O$ (0.52 g) were separately dissolved in 50 mL of distilled water. Subsequently, the aqueous Na_3PO_4 solution was added dropwise under stirring at room temperature to the aqueous $Zn(OAc)_2$ solution. Slow precipitation occurs instantly, indicating the formation of $Zn_3(PO_4)_2(H_2O)_4$. The final product was isolated using the same procedure as used for phosphite. The structural and compositional characterization studies were done by PXRD and ICP-AES analysis.

Instrumental details

X-ray diffraction. PXRD was conducted for the phase identification of the product and was done using a Bruker AXS D8

advanced automatic diffractometer equipped with a position sensitive detector (PSD) and a curved germanium (111) primary monochromator. Cu-$K\alpha$ (λ = 1.5418 Å) radiation was used and the PXRD patterns were recorded in the $5^\circ < 2\theta < 80^\circ$ range. Subsequently, the diffraction pattern fitting was carried out with the program WinXPow and the structural models were drawn with the program DIAMOND version 3.0 using CIF files from the inorganic crystal structure database FINDIT.

Elementary analysis. The compositional ratio of nickel and phosphorous in the precursor was calculated by ICP-AES on a Thermo Jarrell Ash Trace Scan analyzer. The material was dissolved in aqua regia and the results of three independent measurements were averaged to understand the correlation with the chemical formula.

Electron microscopy. To evaluate size and morphology, SEM was used and an EDX analysis was carried out to semi-quantitatively determine the nickel and phosphorus contents in the material. The material was placed on a silicon wafer and the measurements were performed on a LEO DSM 982 microscope integrated with EDX (EDAX, Apollo XPP). The analysis and the data handling were performed with the software package EDAX.

The microstructures of the presented materials were investigated by TEM analysis. A small amount of powder was placed on a TEM-grid (carbon film on a 300 mesh Cu-grid, Plano GmbH, Wetzlar, Germany). The microstructures (morphology, particle size, phase composition, crystallinity) of the samples were studied using an FEI Tecnai G^2 20 S-TWIN transmission electron microscope (FEI Company, Eindhoven, Netherlands) equipped with a LaB_6-source at an acceleration voltage of 200 kV. EDX analysis was conducted with an EDAX r-TEM SUTW Detector (Si(Li)-detector). Images were recorded with a GATAN MS794 P CCD-camera. Both SEM and TEM experiments were carried out at the Zentrum für Elektronenmikroskopie (ZELMI) of the TU Berlin.

FT-IR measurements. The presence of different modes of vibrations of the powder was investigated using a BIORAD FTS 6000 FTIR spectrometer under attenuated total reflection (ATR) conditions. The data were recorded in the 400–4000 cm^{-1} range with an average of thirty-two scans at 4 cm^{-1} resolution.

BET surface area. The surface areas and the pore size distributions were determined on a Quantachrome Autosorb1 apparatus. Nitrogen adsorption/desorption isotherms were determined at −196 °C after degassing the sample at 120 °C overnight. The BET surface areas (S_{BET}) were determined from adsorption data in a relative pressure range from 0.01 to 0.1.

XPS measurements. XPS measurements were performed using a Kratos Axis Ultra X-ray photoelectron spectrometer (Kratos Analytical Ltd, Manchester, UK) using an Al Kα monochromatic radiation source (1486.7 eV) with a take-off angle of 90° (normal to the analyzer). The vacuum pressure in the analyzing chamber was maintained at 2×10^{-9} Torr. The high-resolution XPS spectra were collected for C 1s, O 1s, Ni 2p and P 2p levels with a pass energy of 20 eV and a step of 0.1 eV. The binding energies were calibrated relative to the C 1s peak energy position as 285.0 eV. Data analyses were performed using Casa XPS (Casa Software Ltd) and the Vision data processing program (Kratos Analytical Ltd).

Quasi-*in situ* XAS. The XANES and EXAFS were measured at the BESSY synchrotron radiation source operated by the Helmholtz-Zentrum Berlin. The measurements were performed at the KMC-3 bending-magnet beamline at 20 K in a helium-flow cryostat (Oxford-Danfysik). The incident beam energy was selected by a Si(111) double-crystal monochromator. The measurements at the nickel K-edge were performed in fluorescence mode using a 13-element energy-resolving Ge detector (Canberra) cooled with liquid nitrogen. The extracted spectra were weighted by k^3 and simulated in k-space (E_0 = 8333 eV). All EXAFS simulations were performed using in-house software (SimXLite) after calculation of the phase functions with the FEFF program (version 8.4, self-consistent field option activated). The data range used in the simulation of the EXAFS spectra was k = (3–14) $Å^{-1}$. The EXAFS simulation was optimized by a minimization of the error sum obtained by summation of the squared deviations between measured and simulated values (least-squares fit). The fit was performed using the Levenberg–Marquardt method with numerical derivatives. The error ranges of the fit parameters were estimated from the covariance matrix of the fit. Further details are given elsewhere.[67,76,77] The amplitude reduction factor S_0^2 was kept constant at 1.0 as suggested by test simulations. For the calculation of the phase functions, a fragment (119 atoms) of the nickel phosphite crystal structure was used, including 74 oxygen atoms, 30 nickel atoms and 15 phosphorus atoms.

Materials for XAS experiments were prepared on fluorinated tin oxide substrates in analogy to the electrochemical experiments. After the desired electrochemical OER CA or HER CA measurement, the samples were immediately freeze-quenched using liquid N_2 under vigorous N_2 gas flow and stored in liquid N_2 until the XAS measurements were performed.

Gas chromatography. An Agilent 7890A gas chromatograph (GC) was used to determine the hydrogen and oxygen contents in the headspace. The GC was equipped with a carboxen-1000 column and a thermal conductivity detector (TCD). The carrier gas was argon (Ar). The catalysts were first immersed in the 53 mL closed electrolyzer set-up and bubbled with Ar for 1 h. Subsequently, the gas in the headspace was taken with a syringe and injected into the GC. After the experiments, the amounts of H_2 and O_2 collected in the head-space were determined. The aerial O_2 contribution during sampling was corrected by estimating O_2 before and after the electrochemical reaction.

Mass spectrometric measurements. The head space gas samples were detected using a quadrupole mass spectrometer (InProcess Instruments, Model GAM 200). Helium was considered as an internal standard to quantify the products.

Electrochemical measurements

All electrodes used for the bifunctional OER and HER were prepared by electrophoretic deposition with a potential difference of 10 V in a mixture of iodine and acetone on a 1×1 cm^2 area of FTO (Sigma-Aldrich, resistivity 8–12 Ω sq^{-1}) and NF (Racemat BV). The loading on each FTO electrode was found to

be $\sim$1 mg cm^{-2}, whereas the loading on each NF electrode was $\sim$3 mg cm^{-2}, when deposited for a period of 3 min. The catalytic activities for both the OER and HER were measured in aqueous 1 M KOH solution at room temperature using a single compartment three-electrode electrochemical cell (catalyst deposited on FTO glass serves as the working electrode, Pt wire as the counter electrode, and Hg/Hg_2SO_4 as the reference electrode) with a potentiostat (SP-200, BioLogic Science Instruments) controlled by the EC-Lab v10.20 software package. Cyclic voltammetry (CV) and linear sweep voltammetry (LSV) were carried out with the typical electrolyte resistance (including the electrode) of about 40 Ω; an iR compensation of 80% was applied. The solution was not stirred during the experiments. The potentials presented in this work were referenced to the reversible hydrogen electrode (RHE) through RHE calibration, and in 1 M KOH at pH 14, $E(\mathrm{RHE}) = E(Hg/Hg_2SO_4) + 0.82$ V. The CA measurements were performed in aqueous 1 M KOH at selected constant potentials *vs.* RHE (maintaining a current density of 10 mA cm^{-2}). Freshly prepared materials were used for each OER and HER measurement.

The overall water-splitting reaction was performed in a two-electrode configuration on catalysts deposited on NF and the CA experiments were carried out similar to the HER and OER. The Faradic efficiency and the relative evolution of H_2 and O_2 during each half reaction (*i.e.* the HER and OER) were calculated by following the electrolysis in a closed electrochemical cell and estimation of the respective gases evolved (ESI†).

Conflicts of interest

There are no conflicts to declare.

Acknowledgements

Financial support from the Deutsche Forschungsgemeinschaft (Cluster of Excellence UniCat, EXC 314-2; Priority Program SPP 1613, DA 402/7-2) is gratefully acknowledged. C. P. gratefully acknowledges the Alexander von Humboldt Foundation for a postdoctoral fellowship (2015–2017). The XAS experiments were performed at the BESSY synchrotron (KMC-3 beamline) operated by the Helmholtz-Zentrum Berlin (HZB); we thank the HZB and specifically Dr Ivo Zizak for support. The authors would like to thank Dr Vitaly Gutkin for XPS measurements.

Notes and references

1 T. R. Cook, D. K. Dogutan, S. Y. Reece, Y. Surendranath, T. S. Teets and D. G. Nocera, *Chem. Rev.*, 2010, **110**, 6474–6502.
2 J. Suntivich, K. J. May, H. A. Gasteiger, J. B. Goodenough and Y. Shao-Horn, *Science*, 2011, **334**, 1383–1385.
3 H. B. Gray, *Nat. Chem.*, 2009, **1**, 7.
4 S. Chu and A. Majumdar, *Nature*, 2012, **488**, 294–303.
5 I. Roger, M. A. Shipman and M. D. Symes, *Nat. Rev. Chem.*, 2017, **1**, 0003.
6 P. W. Menezes, A. Indra, P. Littlewood, M. Schwarze, C. Göbel, R. Schomäcker and M. Driess, *ChemSusChem*, 2014, **7**, 2202–2211.
7 A. Indra, P. W. Menezes, I. Zaharieva, E. Baktash, J. Pfrommer, M. Schwarze, H. Dau and M. Driess, *Angew. Chem., Int. Ed.*, 2013, **52**, 13206–13210.
8 M. S. Dresselhaus and I. L. Thomas, *Nature*, 2001, **414**, 332–337.
9 C. C. L. McCrory, S. Jung, I. M. Ferrer, S. M. Chatman, J. C. Peters and T. F. Jaramillo, *J. Am. Chem. Soc.*, 2015, **137**, 4347–4357.
10 C. C. L. McCrory, S. H. Jung, J. C. Peters and T. F. Jaramillo, *J. Am. Chem. Soc.*, 2013, **135**, 16977–16987.
11 Y. Jiao, Y. Zheng, M. T. Jaroniec and S. Z. Qiao, *Chem. Soc. Rev.*, 2015, **44**, 2060–2086.
12 A. Indra, P. W. Menezes, F. Schuster and M. Driess, *J. Photochem. Photobiol., B*, 2015, **152**, 156–161.
13 Y. Lee, J. Suntivich, K. J. May, E. E. Perry and Y. Shao-Horn, *J. Phys. Chem. Lett.*, 2012, **3**, 399–404.
14 J. Greeley, T. F. Jaramillo, J. Bonde, I. B. Chorkendorff and J. K. Norskov, *Nat. Mater.*, 2006, **5**, 909–913.
15 S. Cherevko, S. Geiger, O. Kasian, N. Kulyk, J. P. Grote, A. Savan, B. R. Shrestha, S. Merzlikin, B. Breitbach, A. Ludwig and K. J. J. Mayrhofer, *Catal. Today*, 2016, **262**, 170–180.
16 T. Reier, M. Oezaslan and P. Strasser, *ACS Catal.*, 2012, **2**, 1765–1772.
17 S. Anantharaj, S. R. Ede, K. Sakthikumar, K. Karthick, S. Mishra and S. Kundu, *ACS Catal.*, 2016, **6**, 8069–8097.
18 P. Xiao, W. Chen and X. Wang, *Adv. Energy Mater.*, 2015, **5**, 1500985.
19 M. Gong, D. Y. Wang, C. C. Chen, B. J. Hwang and H. J. Dai, *Nano Res.*, 2016, **9**, 28–46.
20 Q. Zhao, Z. Yan, C. Chen and J. Chen, *Chem. Rev.*, 2017, **117**, 10121–10211.
21 M. M. Najafpour, G. Renger, M. Holynska, A. N. Moghaddam, E. M. Aro, R. Carpentier, H. Nishihara, J. J. Eaton-Rye, J. R. Shen and S. I. Allakhverdiev, *Chem. Rev.*, 2016, **116**, 2886–2936.
22 S. Y. Tee, K. Y. Win, W. S. Teo, L. D. Koh, S. H. Liu, C. P. Teng and M. Y. Han, *Adv. Sci.*, 2017, **4**, 1600337.
23 P. C. K. Vesborg, B. Seger and I. Chorkendorff, *J. Phys. Chem. Lett.*, 2015, **6**, 951–957.
24 Y. M. Shi and B. Zhang, *Chem. Soc. Rev.*, 2016, **45**, 1529–1541.
25 N. T. Suen, S. F. Hung, Q. Quan, N. Zhang, Y. J. Xu and H. M. Chen, *Chem. Soc. Rev.*, 2017, **46**, 337–365.
26 M. Crespo-Quesada and E. Reisner, *Energy Environ. Sci.*, 2017, **10**, 1116–1127.
27 H. Dau, C. Limberg, T. Reier, M. Risch, S. Roggan and P. Strasser, *ChemCatChem*, 2010, **2**, 724–761.
28 J. H. Wang, W. Cui, Q. Liu, Z. C. Xing, A. M. Asiri and X. P. Sun, *Adv. Mater.*, 2016, **28**, 215–230.
29 M. S. Burke, L. J. Enman, A. S. Batchellor, S. H. Zou and S. W. Boettcher, *Chem. Mater.*, 2015, **27**, 7549–7558.
30 L. Liao, S. N. Wang, J. J. Xiao, X. J. Bian, Y. H. Zhang, M. D. Scanlon, X. L. Hu, Y. Tang, B. H. Liu and H. H. Girault, *Energy Environ. Sci.*, 2014, **7**, 387–392.

31 C. Panda, P. W. Menezes, C. Walter, S. Yao, M. E. Miehlich, V. Gutkin, K. Meyer and M. Driess, *Angew. Chem., Int. Ed.*, 2017, **56**, 10506–10510.
32 M. W. Kanan, Y. Surendranath and D. G. Nocera, *Chem. Soc. Rev.*, 2009, **38**, 109–114.
33 M. W. Kanan and D. G. Nocera, *Science*, 2008, **321**, 1072–1075.
34 M. Risch, V. Khare, I. Zaharieva, L. Gerencser, P. Chernev and H. Dau, *J. Am. Chem. Soc.*, 2009, **131**, 6936–6937.
35 Y. Zhan, M. H. Lu, S. L. Yang, Z. L. Liu and J. Y. Lee, *ChemElectroChem*, 2016, **3**, 615–621.
36 Y. B. Li and C. Zhao, *Chem. Mater.*, 2016, **28**, 5659–5666.
37 I. Paseka, *Electrochim. Acta*, 1995, **40**, 1633–1640.
38 M. J. Giz, G. Tremiliosi-Filho, E. R. Gonzalez, S. Srinivasan and A. J. Appleby, *Int. J. Hydrogen Energy*, 1995, **20**, 423–427.
39 C. C. Hu and A. Bai, *J. Appl. Electrochem.*, 2001, **31**, 565–572.
40 T. Burchardt, V. Hansen and T. Valand, *Electrochim. Acta*, 2001, **46**, 2761–2766.
41 E. J. Popczun, J. R. McKone, C. G. Read, A. J. Biacchi, A. M. Wiltrout, N. S. Lewis and R. E. Schaak, *J. Am. Chem. Soc.*, 2013, **135**, 9267–9270.
42 L. A. Stern, L. G. Feng, F. Song and X. L. Hu, *Energy Environ. Sci.*, 2015, **8**, 2347–2351.
43 B. You, N. Jiang, M. L. Sheng, M. W. Bhushan and Y. J. Sun, *ACS Catal.*, 2016, **6**, 714–721.
44 J. Y. Li, J. Li, X. M. Zhou, Z. M. Xia, W. Gao, Y. Y. Ma and Y. Q. Qu, *ACS Appl. Mater. Interfaces*, 2016, **8**, 10826–10834.
45 X. G. Wang, W. Li, D. H. Xiong, D. Y. Petrovykh and L. F. Liu, *Adv. Funct. Mater.*, 2016, **26**, 4067–4077.
46 G. F. Chen, T. Y. Ma, Z. Q. Liu, N. Li, Y. Z. Su, K. Davey and S. Z. Qiao, *Adv. Funct. Mater.*, 2016, **26**, 3314–3323.
47 N. Jiang, B. You, M. L. Sheng and Y. J. Sun, *ChemCatChem*, 2016, **8**, 106–112.
48 M. Ledendecker, S. K. Calderon, C. Papp, H. P. Steinruck, M. Antonietti and M. Shalom, *Angew. Chem., Int. Ed.*, 2015, **54**, 12361–12365.
49 R. Zhang, P. A. Russo, M. Feist, P. Amsalem, N. Koch and N. Pinna, *ACS Appl. Mater. Interfaces*, 2017, **9**, 14013–14022.
50 P. W. Menezes, A. Indra, C. Das, C. Walter, C. Gobel, V. Gutkin, D. Schmeisser and M. Driess, *ACS Catal.*, 2017, **7**, 103–109.
51 M. D. Marcos, P. Amoros, A. Beltranporter, R. Martinezmanez and J. P. Attfield, *Chem. Mater.*, 1993, **5**, 121–128.
52 Y. P. Gao, J. H. Zhao, Z. Run, G. Q. Zhang and H. Pang, *Dalton Trans.*, 2014, **43**, 17000–17005.
53 H. Pang, C. Z. Wei, Y. H. Ma, S. S. Zhao, G. C. Li, J. S. Zhang, J. Chen and S. J. Li, *ChemPlusChem*, 2013, **78**, 546–553.
54 D. H. Lee, M. Kang, S. M. Paek and H. Jung, *Bull. Korean Chem. Soc.*, 2016, **37**, 192–199.
55 M. C. Biesinger, B. P. Payne, L. W. M. Lau, A. Gerson and R. S. C. Smart, *Surf. Interface Anal.*, 2009, **41**, 324–332.
56 Z. J. Gu, T. Y. Zhai, B. F. Gao, G. J. Zhang, D. M. Ke, Y. Ma and J. N. Yao, *Cryst. Growth Des.*, 2007, **7**, 825–830.
57 E. L. Ratcliff, J. Meyer, K. X. Steirer, A. Garcia, J. J. Berry, D. S. Ginley, D. C. Olson, A. Kahn and N. R. Armstrong, *Chem. Mater.*, 2011, **23**, 4988–5000.
58 H. Q. Zhou, F. Yu, Y. F. Huang, J. Y. Sun, Z. Zhu, R. J. Nielsen, R. He, J. M. Bao, W. A. Goddard, S. Chen and Z. F. Ren, *Nat. Commun.*, 2016, **7**, 12765.
59 X. Y. Lu and C. A. Zhao, *Nat. Commun.*, 2015, **6**, 6616.
60 X. G. Wang, Y. V. Kolen'ko, X. Q. Bao, K. Kovnir and L. F. Liu, *Angew. Chem., Int. Ed.*, 2015, **54**, 8188–8192.
61 A. Dutta and N. Pradhan, *J. Phys. Chem. Lett.*, 2017, **8**, 144–152.
62 L. Trotochaud, S. L. Young, J. K. Ranney and S. W. Boettcher, *J. Am. Chem. Soc.*, 2014, **136**, 6744–6753.
63 L. Trotochaud, J. K. Ranney, K. N. Williams and S. W. Boettcher, *J. Am. Chem. Soc.*, 2012, **134**, 17253–17261.
64 P. W. Menezes, A. Indra, O. Levy, K. Kailasam, V. Gutkin, J. Pfrommer and M. Driess, *Chem. Commun.*, 2015, **51**, 5005–5008.
65 H. Q. Zhou, F. Yu, J. Y. Sun, R. He, S. Chen, C. W. Chu and Z. F. Ren, *Proc. Natl. Acad. Sci. U. S. A.*, 2017, **114**, 5607–5611.
66 M. Gorlin, J. F. de Araujo, H. Schmies, D. Bernsmeier, S. Dresp, M. Gliech, Z. Jusys, P. Chernev, R. Kraehnert, H. Dau and P. Strasser, *J. Am. Chem. Soc.*, 2017, **139**, 2070–2082.
67 M. Risch, F. Ringleb, M. Kohlhoff, P. Bogdanoff, P. Chernev, I. Zaharieva and H. Dau, *Energy Environ. Sci.*, 2015, **8**, 661–674.
68 W. T. Hong, M. Risch, K. A. Stoerzinger, A. Grimaud, J. Suntivich and Y. Shao-Horn, *Energy Environ. Sci.*, 2015, **8**, 1404–1427.
69 M. Zhang, M. de Respinis and H. Frei, *Nat. Chem.*, 2014, **6**, 362–367.
70 E. Fabbri, A. Habereder, K. Waltar, R. Kotz and T. J. Schmidt, *Catal. Sci. Technol.*, 2014, **4**, 3800–3821.
71 F. Dionigi and P. Strasser, *Adv. Energy Mater.*, 2016, **6**, 1600621.
72 X. Xu, F. Song and X. L. Hu, *Nat. Commun.*, 2016, **7**, 12324.
73 P. W. Menezes, A. Indra, A. Bergmann, P. Chernev, C. Walter, H. Dau, P. Strasser and M. Driess, *J. Mater. Chem. A*, 2016, **4**, 10014–10022.
74 A. Davidson, J. F. Tempere, M. Che, H. Roulet and G. Dufour, *J. Phys. Chem.*, 1996, **100**, 4919–4929.
75 P. M. A. Sherwood, *Surf. Sci. Spectra*, 2002, **9**, 62–66.
76 I. Zaharieva, D. Gonzalez-Flores, B. Asfari, C. Pasquini, M. R. Mohammadi, K. Klingan, I. Zizak, S. Loos, P. Chernev and H. Dau, *Energy Environ. Sci.*, 2016, **9**, 2433–2443.
77 D. Gonzalez-Flores, I. Zaharieva, J. Heidkamp, P. Chernev, E. Martinez-Moreno, C. Pasquini, M. R. Mohammadi, K. Klingan, U. Gernet, A. Fischer and H. Dau, *ChemSusChem*, 2016, **9**, 379–387.
78 M. Gorlin, P. Chernev, J. F. de Araujo, T. Reier, S. Dresp, B. Paul, R. Krahnert, H. Dau and P. Strasser, *J. Am. Chem. Soc.*, 2016, **138**, 5603–5614.
79 M. K. Bates, Q. Y. Jia, N. Ramaswamy, R. J. Allen and S. Mukerjee, *J. Phys. Chem. C*, 2015, **119**, 5467–5477.
80 C. Y. He, X. L. Wu and Z. Q. He, *J. Phys. Chem. C*, 2014, **118**, 4578–4584.
81 N. Danilovic, R. Subbaraman, D. Strmcnik, K. C. Chang, A. P. Paulikas, V. R. Stamenkovic and N. M. Markovic, *Angew. Chem., Int. Ed.*, 2012, **51**, 12495–12498.

82 K. K. Bando, Y. Koike, T. Kawai, G. Tateno, S. T. Oyama, Y. Inada, M. Nomura and K. Asakura, *J. Phys. Chem. C*, 2011, **115**, 7466–7471.
83 J. F. Callejas, C. G. Read, C. W. Roske, N. S. Lewis and R. E. Schaak, *Chem. Mater.*, 2016, **28**, 6017–6044.
84 D. H. Ha, B. H. Han, M. Risch, L. Giordano, K. P. C. Yao, P. Karayaylali and Y. Shao-Horn, *Nano Energy*, 2016, **29**, 37–45.
85 A. Indra, P. W. Menezes, K. Kailasam, D. Hollmann, M. Schroder, A. Thomas, A. Bruckner and M. Driess, *Chem. Commun.*, 2016, **52**, 104–107.
86 A. Indra, A. Acharjya, P. W. Menezes, C. Merschjann, D. Hollmann, M. Schwarze, M. Aktas, A. Friedrich, S. Lochbrunner, A. Thomas and M. Driess, *Angew. Chem., Int. Ed.*, 2017, **56**, 1653–1657.
87 L. Wang, C. Lin, D. K. Huang, J. M. Chen, L. Jiang, M. K. Wang, L. F. Chi, L. Shi and J. Jin, *ACS Catal.*, 2015, **5**, 3801–3806.
88 M. Gong, W. Zhou, M. C. Tsai, J. G. Zhou, M. Y. Guan, M. C. Lin, B. Zhang, Y. F. Hu, D. Y. Wang, J. Yang, S. J. Pennycook, B. J. Hwang and H. J. Dai, *Nat. Commun.*, 2014, **5**, 4695.
89 Q. Li, Z. C. Xing, D. W. Wang, X. P. Sun and X. R. Yang, *ACS Catal.*, 2016, **6**, 2797–2801.
90 R. Subbaraman, D. Tripkovic, D. Strmcnik, K. C. Chang, M. Uchimura, A. P. Paulikas, V. Stamenkovic and N. M. Markovic, *Science*, 2011, **334**, 1256–1260.
91 Y. Wu, J. Jiang, Z. Weng, M. Wang., D. Broere, Y. Zhong, G. Brudvig, Y. Feng and H. Wang, *ACS Cent. Sci.*, 2017, **3**, 847–852.
92 M. M. Khusniyarov, E. Bill, T. Weyhermuller, E. Bothe and K. Wieghardt, *Angew. Chem., Int. Ed.*, 2011, **50**, 1652–1655.
93 B. M. Hunter, W. Hieringer, J. R. Winkler, H. B. Gray and A. M. Muller, *Energy Environ. Sci.*, 2016, **9**, 1734–1743.
94 L. Yu, H. Q. Zhou, J. Y. Sun, F. Qin, F. Yu, J. M. Bao, Y. Yu, S. Chen and Z. F. Ren, *Energy Environ. Sci.*, 2017, **10**, 1820–1827.
95 M. R. Gao, W. C. Sheng, Z. B. Zhuang, Q. R. Fang, S. Gu, J. Jiang and Y. S. Yan, *J. Am. Chem. Soc.*, 2014, **136**, 7077–7084.
96 H. Kim, J. Park, I. Park, K. Jin, S. E. Jerng, S. H. Kim, K. T. Nam and K. Kang, *Nat. Commun.*, 2015, **6**, 8253.
97 X. Y. Yu, Y. Feng, B. Y. Guan, X. W. Lou and U. Paik, *Energy Environ. Sci.*, 2016, **9**, 1246–1250.
98 C. Tang, N. Y. Cheng, Z. H. Pu, W. Xing and X. P. Sun, *Angew. Chem., Int. Ed.*, 2015, **54**, 9351–9355.
99 A. Indra, P. W. Menezes, N. R. Sahraie, A. Bergmann, C. Das, M. Tallarida, D. Schmeisser, P. Strasser and M. Driess, *J. Am. Chem. Soc.*, 2014, **136**, 17530–17536.
100 J. Pfrommer, M. Lublow, A. Azarpira, C. Gobel, M. Lucke, A. Steigert, M. Pogrzeba, P. W. Menezes, A. Fischer, T. Schedel-Niedrig and M. Driess, *Angew. Chem., Int. Ed.*, 2014, **53**, 5183–5187.
101 Y. Yan, B. Y. Xia, B. Zhao and X. Wang, *J. Mater. Chem. A*, 2016, **4**, 17587–17603.

